JOURNAL OF AIRCRAFT
Vol. 44, No. 1, January–February 2007

Automatic Transition Prediction and Application to Three-Dimensional Wing Configurations

Andreas Krumbein*
DLR, German Aerospace Center, 37073 Göttingen, Germany

DOI: 10.2514/1.22254

A Reynolds-averaged Navier–Stokes solver, a laminar boundary-layer code and two e^N-database methods for the prediction of transition due to Tollmien–Schlichting and crossflow instabilities were coupled to perform Reynolds-averaged Navier–Stokes computations of three-dimensional, finite wings with automatic laminar-turbulent transition prediction. It will be shown, that the coupled system represents a Reynolds-averaged Navier–Stokes-based computational fluid dynamics tool that provides accurate values of the transition locations during the ongoing Reynolds-averaged Navier–Stokes computation automatically and fast without the need for the intervention by the code user. Thus, Reynolds-averaged Navier–Stokes computations of three-dimensional wing configurations with transition can be carried out without a priori knowledge of the transition characteristics of the specific flow problem. The coupling structure and the underlying algorithm of the transition prediction procedure and the functioning of the e^N-database methods are described. The testing of the transition prediction procedure is described and documented. The computational results are compared with experimental data.

Nomenclature

A = aspect ratio
b = semispan
C^T = underrelaxation factor
$C^{T,i}$ = initial value of the underrelaxation factor
c_d = drag coefficient
c_f = skin friction coefficient
c_l = lift coefficient
c_m = mean aerodynamic chord
c_p = pressure coefficient
$\boldsymbol{e}$ = unity vector
F = reduced frequency, $F = 2\pi f \mu_e / \left(\rho_e U_e^2\right) = \omega \nu_e / U_e^2$
f = frequency
H_i = incompressible shape parameter, $H_i = \delta_i^* / \Theta_i$
k = turbulent kinetic energy or number of Reynolds-averaged Navier–Stokes cycles for the transition location iteration which represents the interval between two calls of the transition prediction module
$\boldsymbol{k}$ = wave number vector
M = Mach number
$N|_{x^T}$ = limiting N-factor at the transition location x^T
n_T = global number of transition points
P = point of the computational grid
P_S = surface point of the computational grid
P_{infl} = measure for the shear stress at the inflection point
R = specific gas constant, R = 287.4 [J/(kg K)] for air
Re_l = Reynolds number based on the length l, that is, $U_e l / \nu_e$
Tu = turbulence intensity
t = time
U = tangential, chordwise flow velocity
U_e = tangential, chordwise flow velocity at the boundary-layer edge
v = absolute value of mean flow velocity vector
$\boldsymbol{v}$ = mean flow velocity vector
$\boldsymbol{v}'$ = perturbation of the velocity vector
$\boldsymbol{v}_g$ = group velocity vector
W = tangential, spanwise flow velocity
x = longitudinal coordinate of the configuration in the global coordinate system of the Reynolds-averaged Navier–Stokes solver or tangential, chordwise direction of the local coordinate system originating in a surface point
x' = coordinate of the local, external streamline direction
x_0 = x-coordinate of the point where a perturbation enters the unstable zone
x^T = longitudinal coordinate value of the transition point
$\tilde{x}^T$ = longitudinal coordinate value of the transition point, underrelaxed
y = vertical coordinate of the configuration in the global coordinate system of the Reynolds-averaged Navier–Stokes solver or wall normal direction of the local coordinate system originating in a surface point
z = tangential, spanwise coordinate whose direction is orthogonal to the tangential, chordwise direction x and the wall normal direction y of the local coordinate system originating in a surface point
z' = coordinate of the second tangential direction perpendicular to the local, external streamline direction x'
α = angle of attack or chordwise wave number
α_i = local spatial amplification rate
β = spanwise wave number
δ = boundary layer thickness
δ_i^* = incompressible displacement thickness,

$$\delta_i^* = \int_0^\delta \left(1 - \frac{U(y)}{U_e}\right) \mathrm{d}y$$

ε = lower limit for convergence criterion
η = nondimensional spanwise coordinate
Θ_i = incompressible momentum loss thickness,

$$\Theta_i = \int_0^\delta \frac{U(y)}{U_e} \left(1 - \frac{U(y)}{U_e}\right) \mathrm{d}y$$

φ = angle denoting an arbitrary direction
κ = ratio of specific heat capacities, $\kappa = 1.4$ for air
Λ = sweep angle
λ = taper ratio

Presented as Paper 0914 at the 44th AIAA Aerospace Sciences Meeting and Exhibit, Reno, Nevada, 9–12 January 2006; received 5 January 2006; revision received 10 July 2006; accepted for publication 10 July 2006.

*Research Scientist, R & D Engineer, Institute of Aerodynamics and Flow Technology, Numerical Methods, Bunsenstraße 10, AIAA Member; andreas.krumbein@dlr.de.

μ_e = dynamic viscosity at the boundary-layer edge
ν_e = kinematic viscosity at the boundary-layer edge
ρ = density
ρ_e = density at the boundary-layer edge
σ = local spatial growth rate, $\sigma = -\alpha_i$
Ψ = wave propagation angle
Ψ_g = group velocity propagation angle
ω = circular frequency or specific turbulent dissipation rate
ω_i = temporal amplification rate
ω_r = circular frequency

Subscripts

AL = attachment line
CF = crossflow
crit = critical
e = element or edge of the boundary layer
eff = effective
$\mathbf{e}_x$ = in chordwise direction
g = group
i = incompressible; imaginary; initial
infl = at inflection point
j = counter of the transition points
$\boldsymbol{k}$ = in direction of the wave number vector
LE = leading edge
l = counter of the transition iteration steps
lim = limiting
m = mean
max = maximum
min = minimum
r = real
S = surface
sec = section
T = transition
TE = trailing edge
TS = Tollmien–Schlichting
x = in x-direction
x' = in x'-direction
z = in z-direction
z' = in z'-direction
Ψ = in wave propagation direction
∞ = freestream value

I. Introduction

THE modeling of laminar-turbulent transition in Reynolds-averaged Navier–Stokes (RANS) solvers is a necessary requirement for the computation of flows over airfoils and wings in the aerospace industry because it is not possible to obtain quantitatively correct results if the laminar-turbulent transition is not taken into account. Especially the simulation of flows around high-lift systems of aircraft may result in significant errors when the transition points are simply estimated or are not taken into account at all. High-lift systems very often involve multicomponent wings (e.g., slat, main wing, and flaps) and usually exhibit very high levels of total circulation. Because all components of the high-lift system are in close interaction with one another, the total circulation and the complete flowfield is affected by one transition line on one of the components.

Although the overall lift value may be predicted with satisfactory accuracy, slight deviations between the real and the computed pressures can lead to large errors in the computed overall drag value. This issue was investigated in detail in [1] and it was shown that the overall pressure drag of a high-lift configuration, which dominates the drag value of the configuration as a whole as well as the drag of every single element, is composed of a balance of very large positive and negative contributions. The contribution of one single element may be one order of magnitude larger than the resulting overall drag of the complete configuration. Thus, a relative error of 5% of the computed drag on the slat upper side may result in a change of 50% for the overall drag value.

For the design process of wings in industry, there exists the demand for a RANS-based computational fluid dynamics (CFD) tool that is able to handle flows automatically and autonomously with laminar-turbulent transition. Existing transition prediction methods vary from empirical transition criteria via the local, linear stability equations based on small disturbance theory or nonlocal, linear and nonlocal, nonlinear stability methods using the parabolized stability equations over large eddy simulations to direct numerical simulations of the Navier–Stokes equations. Empirical transition criteria and the e^N-method [2,3] based on local, linear stability theory and the parallel flow assumption represent state-of-the-art methods for the prediction of transition onset in many industrial applications. Although they do not account for a number of fundamental aspects in the transition process e^N-methods are used in aircraft industry most frequently for design purposes covering transition due to Tollmien–Schlichting and crossflow instabilities. Because there are no other practical methods presently available for industrial applications [4], e^N-methods together with the two-N-factor method and empirical criteria for transition mechanisms which are not covered by the e^N approach (e.g., bypass and attachment line transition) are going to be used further on for the design of aircraft wings and wing systems even for a future laminar wing of transport type aircraft.

The first steps towards the setup of a RANS-based CFD tool with automatic transition prediction were made in [5], where a RANS solver and an e^N-method were applied, and in [6], where a RANS solver, a laminar boundary-layer method [7], and an e^N-method were coupled. There, the boundary-layer method was used to produce highly accurate laminar, viscous layer data to be analyzed by a linear stability code. Hence, the very expensive grid adaptation necessary to produce accurate viscous layer data directly from a structured Navier–Stokes grid was avoided. The use of e^N-database methods [8,9] results in a coupled program system that is able to handle transition prediction automatically. In [10], a database for the growth rates is used which are represented by a trained neural network based on Falkner–Skan–Cooke profiles. Alternative approaches using a transition closure model or a transition/turbulence model directly incorporated into the RANS solver are documented in [11–13]. A correlation-based transition modeling approach built on local variables using transport equations for the intermittency and for a transition onset criterion in terms of the momentum thickness Reynolds number is documented in [14].

At the Deutsches Zentrum für Luft- und Raumfahrt, German Aerospace Center (DLR), the block-structured RANS code FLOWer [15] is used together with the laminar boundary-layer method in [7] and the e^N-database methods in [8,9]. The laminar boundary-layer method and the e^N-database methods form a so-called transition prediction module that is coupled to the RANS solver and that interacts with the RANS solver during the computation [16,17]. Presently, the transition prediction module of the FLOWer code can be applied to two-dimensional one-element or multi-element configurations and to three-dimensional one-element or multi-element wing configurations.

In [18,19], the FLOWer code was applied to two-dimensional multi-element airfoil configurations with transition. In the present paper, the extension of the functionality to three-dimensional, finite wing configurations is described and the first application to a three-dimensional wing is demonstrated for different flow cases. The main objective is to show that the coupling structure between a RANS solver and the transition prediction module can be now applied to three-dimensional wing flows with the same reliability as it was done before for two-dimensional airfoil flows from a technical point of view and that the FLOWer code provides all technical features which are necessary for the transition prediction on wing configurations. Another objective is to point out a shortcoming of the e^N-method when it is applied to configurations tested in a wind tunnel. This shortcoming is inherent in the e^N-method because it is a semi-empirical method which requires the knowledge of the N factors. The N factors have to be determined experimentally, and for wings of transport-type aircraft in free flight, the ranges of values of the N factors for Tollmien–Schlichting and crossflow instabilities were determined in extensive flight test programs. This fact justifies the

application of the e^N-method when free flight configurations are investigated numerically. For wind tunnel flows, however, the N factors must be determined individually for each wind tunnel because their values depend on the specific characteristics of the wind tunnel. Here, difficulties can arise, especially in the case of crossflow instabilities, when the N factors are not known. These difficulties become particularly obvious when validation work must be realized based on experimental test cases which lack sufficient information necessary for the transition prediction or when the experimental data are not clearly interpretable or even contradictory. In these cases, the e^N-method must be calibrated using transition information from the experiment itself. In the end, it will be shown that the coupled system consisting of the FLOWer code and the transition prediction module represents a RANS-based CFD tool that, in principle, provides accurate values of the transition locations on three-dimensional, finite wings during the ongoing RANS computation automatically and fast without the need for the intervention of the user.

The method and the algorithm for the coupling of the transition prediction module and, thereby, for detecting the laminar-turbulent transition locations based on linear stability theory are described. The paper focuses on the structure of the transition prediction module and its coupling to the FLOWer code, the underlying algorithm of the transition prediction procedure [6–8,16,17], the testing of the algorithm, and the application of the prediction procedure to three-dimensional wing flows. The testing is described and documented by a number of commented plots of the results of the transition prediction procedure. The computed values are compared with experimental findings.

II. Implementation

FLOWer is a three-dimensional, compressible RANS code for steady or unsteady flow problems and uses structured body-fitted multiblock meshes. The code is based on a finite volume method and a cell-vertex spatial discretization scheme and uses an explicit Runge–Kutta time integration scheme with multigrid acceleration. The influence of turbulence is taken into account by eddy viscosity turbulence models according to the Boussinesq approximation. The transition handling is independent of the block topology of the computational grid and of the grid structure (structured, unstructured, or hybrid grid) [16].

A. Transition Prediction Coupling and Algorithm

The complete coupled program system that is used for transition prediction with the RANS solver FLOWer consists of the RANS solver itself [15], a laminar boundary-layer method for swept, tapered wings [7], and a transition prediction method, which is provided with all necessary data, for example, boundary-layer parameters such as δ, H_i, and $Re_{\delta_i^*}$, by the laminar boundary-layer method. The laminar boundary-layer method solves the compressible laminar boundary-layer equations for conical external flow using the surface pressure distribution from the stagnation or attachment line point along a wing section as input. It can be applied to unswept and swept infinite or tapered wings with and without heat transfer and suction, and uses finite differences with second order accuracy in streamwise and fourth order accuracy in wall normal direction. Besides a number of empirical transition criteria, the most general transition prediction methods that are available in the FLOWer transition prediction module are an e^N-database method for Tollmien–Schlichting (TS) instabilities [8] and an e^N-database method for crossflow (CF) instabilities [9].

The RANS solver communicates the surface pressure distribution of the configuration as input data to the laminar boundary-layer method, the laminar boundary-layer method computes all of the boundary-layer parameters that are needed for the transition prediction method, and the transition prediction method determines new transition locations that are given back to the RANS solver. This coupled structure results in an iterative procedure for the transition locations within the iteration of the RANS equations. The structure of

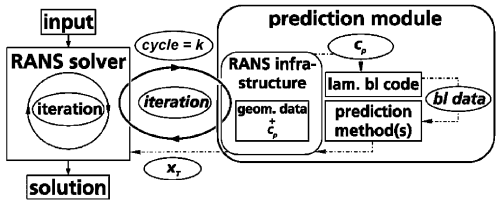

Fig. 1 Transition prediction coupling structure.

the approach is outlined graphically in Fig. 1 (where lam. bl is the laminar boundary layer). After a certain number of iteration cycles k of the RANS solution process, the solver is stopped, the transition prediction module is called, the module analyzes the laminar boundary layers of the upper and lower sides of specified wing sections, and determines transition locations, $x_j^T(\text{cycle} = k)$ with $j = 1, \ldots, n_T$. These locations are communicated back to the RANS solver, which performs transition prescription applying a transition setting algorithm [16,17], and the computation is continued. In so doing, the determination of the transition locations becomes an iteration process itself. At every call of the module, the RANS surface pressure $c_p(k)$ along a wing section is used as input for the transition prediction module. The viscous data calculated by the boundary-layer method are subsequently analyzed by the e^N-database methods.

The application of a boundary-layer method for the computation of all viscous data necessary for the transition prediction method ensures the high accuracy of the viscous data required by the e^N-methods for the analysis of laminar boundary layers. Thus, as shown in [6], the large number of grid points near the wall for a high resolution of the boundary layers, the adaptation of the Navier–Stokes grid in the laminar, turbulent and transitional boundary-layer regions, and the generation of new adapted grids for the RANS solver after every step of the transition location iteration are avoided and the computational time can be massively reduced. In addition, the number of RANS iteration cycles between two steps of the transition location iteration can be highly reduced compared with an approach where the boundary-layer parameters are computed directly from the RANS grid [20,21], because the surface pressure converges significantly faster in the RANS computation than the boundary-layer velocity profiles [22] which are the basis for the computation of the boundary-layer parameters. The algorithm for the transition prediction iteration works as follows:

1) The RANS solver is started as if a computation with prescribed transition locations is to be performed. At this stage, the transition locations are set very far downstream on the upper and lower sides of the wing sections, for example, at the trailing edges. The RANS solver then initially computes a fully laminar flow or a flow with large laminar regions over the wing.

2) During the solution process of the RANS equations the laminar flow regions are checked for laminar separation points by the RANS solver. In the case that a laminar separation is detected, the separation point is used as an approximation of the transition location, the transition is fixed there, and the computation is continued.

3) The RANS equations are iterated until the lift coefficient $c_l = c_l(\text{cycle})$ has become constant with respect to the iteration cycles.

4) The transition prediction module is called. The laminar boundary-layer method determines the locations of laminar separation on upper and lower sides of each wing section. The e^N-database methods determine the transition locations on upper and lower sides of each wing section. In the case that the e^N-database methods do not detect transition locations due to Tollmien–Schlichting instabilities or due to crossflow instabilities upstream of the current laminar separation point from the boundary-layer method, the laminar separation point is used as an approximation of the real transition point and transition is fixed there.

5) The current coordinate $x_j^T(k)$, which is used as a transition location, is underrelaxed. That is, as new transition locations the coordinates $\tilde{x}_j^T(k)$, which are located downstream of the coordinates $x_j^T(k)$, are used according to

$$\tilde{x}_j^T(k) = C_j^T(k) x_j^T(k) \qquad \text{with} \qquad j = 1, \ldots, n_T \tag{1}$$

with $C_j^T(k) > 1$. Only after the last step of the transition location iteration $C_j^T(k) = 1$ is applied.

6) As convergence criterion,

$$\Delta\tilde{x}_j^{T,l} < \varepsilon \approx 1\% \qquad \text{with} \qquad \Delta\tilde{x}_j^{T,l} = |\tilde{x}_j^T(k^l) - \tilde{x}_j^T(k^{l-1})| \tag{2}$$

is applied, where l is the current iteration step. In the case that the criterion is satisfied, the iteration for x_j^T is finished, else the algorithm loops back to station 2.

Part 2 of the algorithm (the use of the RANS laminar separation points as approximations of the transition locations) is a technique to stabilize the RANS computation and to prevent large laminar separation regions in a computation where the transition points have not yet reached their converged position. The points of laminar separation which occur during the transient phase of the RANS computation and which are used as transition points until the transition prediction module is called are moving from the trailing edge towards the leading edge of each wing section. This movement is one aspect of the continuously changing intermediate solutions of the flowfield which are iterated towards a converged steady state by the computational procedure of the RANS solver. How the separation points are detected in the RANS computational grid during the transient phase of the RANS computation is described in detail in [18].

Part 3 of the algorithm ensures that numerical disturbances which are still present during the transient phase of the RANS computation have been reduced to a low level before a stability analysis of the boundary layers is performed. Thus, the stability analysis is free from artificial disturbances. This is essential because the surface pressure (the surface pressure distribution is the basis for all laminar boundary-layer parameters which are provided by the laminar boundary-layer method and which are then analyzed by the e^N-database methods) is heavily disturbed in the transient phase and directly affects the lift coefficient. Thus, the lift coefficient is used as a criterion for the decision if a stability analysis should be carried out or not.

Whereas part 2 of the algorithm is used to stabilize the RANS computation, the approximation of the real transition points by laminar separation point in part 4 is the attempt to predict transition due strictly to the presence of separation bubbles. This approach often yields a good approximation of the real transition point when transition does not occur before the laminar boundary layer separates, particularly for low Reynolds number flows.

The underrelaxation technique in part 5 is a procedure to damp oscillations in the convergence history of the transition locations to obtain a smooth movement of the transition locations from the trailing edge towards the leading edge of each wing section. It prevents the case that at an unconverged stage during the transition location iteration, transition coordinates which are determined too far upstream might not be shifted downstream again. For the value of the underrelaxation factor

$$C_j^T(k) = x_j^T(k^l) + C^{T,i}|\tilde{x}_j^T(k^{l-1}) - x_j^T(k^l)| \tag{3}$$

is used, where l is the current iteration step and $C^{T,i}$ is an initial value of the underrelaxation factor given as input parameter by the user of the code. Thus, it is ensured that the value of the underrelaxation factor becomes smaller and smaller during the transition location iteration. In the case that the convergence criterion from part 6 is satisfied $C_j^T(k) = 1$ is applied.

This transition location iteration procedure was very successfully applied to single- and multi-element airfoil flows involving regions with adverse as well as favorable pressure gradients, and cases with slow as well as quick growth of the Tollmien–Schlichting waves in [16,17,23–26]. In [17], it was shown that the final values of the converged transition locations are independent of the values of the initial transition locations. The same independence can be read for multi-element airfoils in [24].

The definition of a wing section is given by the boundary-layer edge streamlines running over the upper and lower sides of the wing, originating in the boundary-layer edge point associated with the stagnation point (in two-dimensional problems) or attachment line point (in three-dimensional problems) on the wing surface in the area of the oncoming flow. At the moment, the FLOWer code is not yet capable of computing streamlines. Thus, a wing section is approximated by a surface grid line of the block-structured grid. The grid lines on the wing surface have to be well parallel and more or less perpendicular to the leading and trailing edges of the wing.

B. Transition Modeling

The e^N-method for Tollmien–Schlichting instabilities [8] applies

$$N|_{x^T} = -\int_{x_0}^{x^T} \alpha_i \, \mathrm{d}x \tag{4}$$

as transition criterion and expresses α_i in the form

$$\alpha_i = \alpha_i(H_i, Re_{\delta_i^*}, F) \tag{5}$$

As described in [8,27], Falkner–Skan boundary-layer profiles were generated for 13 shape parameters H_i, which cover the range from highly accelerated up to separating flows. The growth of the boundary layer was simulated by varying $Re_{\delta_i^*}$. For each boundary layer, stability computations were completed for a sufficient large range of excited frequencies. The results for the amplification rates α_i were stored in a database. The stability computation for a real boundary layer is then executed for a given frequency f [Hz = 1/s] in the following way: at each grid point on the wing section the properties f, $Re_{\delta_i^*}$, H_i, U_e, μ_e, and ρ_e are known. Evaluating F from the value of f, α_i is obtained from Eq. (5) via interpolation in the database. For compressible flows, the relationships in Eq. (5) were extended by four levels of the Mach number at the boundary-layer edge M_e covering the range $0 \le M_e \le 1.4$.

For the application of the e^N-method, extensive experimental programs have been performed to determine the value of $N|_{x^T}$ which depends on the environmental disturbances in the flow. For free-flight conditions $N|_{x^T} \approx 12$ was found for Tollmien–Schlichting waves. For wind tunnel conditions, Mack's relationship

$$N|_{x^T} = -8.43 - 2.4 \ln(Tu_\infty) \tag{6}$$

can be applied with some confidence.

The e^N-method for crossflow instabilities used [9] has been developed at ONERA by Casalis and Arnal and is based on a simplified approach originally developed for two-dimensional flows [28,29]. There, for a prescribed value of the reduced frequency F and a given velocity profile, the curve of the local spatial growth rate $\sigma = -\alpha_i$ as a function of $Re_{\delta_i^*}$ is approximated by two half-parabolas

$$\frac{\sigma}{\sigma_M} = 1 - \left[\frac{Re_{\delta_i^*} - Re_{\delta_i^* M}}{Re_{\delta_i^* k} - Re_{\delta_i^* M}}\right]^2 \qquad \text{with}$$
$$k = \begin{cases} 0 & \text{if } Re_{\delta_i^*} < Re_{\delta_i^* M} \\ 1 & \text{if } Re_{\delta_i^*} > Re_{\delta_i^* M} \end{cases} \tag{7}$$

where $Re_{\delta_i^* k}$, $k = 0, 1$ denote the zeros of the left ("0") and right ("1") half-parabola, and the pair $[\sigma_M, Re_{\delta_i^* M}]$ denotes the zenith where the two half-parabolas meet. The variations of these parameters are approximated by simple, algebraic relationships such as $Re_{\delta_i^* M} = KF^E$, where K, E, and the coefficients appearing in the corresponding expressions for the other parameters are constant for a prescribed velocity profile and depend only on the shape of the velocity profile. The values of these coefficients were tabulated as functions of the incompressible shape parameter H_i and have been determined by exact stability computations for Falkner–Skan solutions.

For separated flows, the coefficients become dependent on parameters different than H_i. For a wide range of velocity profiles with reverse flow, whose instability type is essentially inflectional,

the parameters are related to characteristics of the inflection point 1) the mean velocity at the inflection point $(U/U_e)_{\text{infl}}$, and 2) a measure for the shear stress at the inflection point

$$P_{\text{infl}} = \left[\frac{y}{\delta}\frac{d(U(y)/U_e)}{d(y/\delta)}\right]_{\text{infl}}$$

Determining H_i, $(U/U_e)_{\text{infl}}$, and P_{infl} from computed velocity profiles, the coefficients can be calculated evaluating the algebraic relationships for $Re_{\delta_i^* k}$, $k = 0, 1$, $Re_{\delta_i^* M}$, and σ_M. Then $Re_{\delta_i^* k}$, $k = 0$, 1, $Re_{\delta_i^* M}$, and σ_M themselves can be calculated for the range of unstable frequencies. For each frequency, σ is computed from Eq. (7). Then the integration of σ in chordwise direction is performed to determine the N factor curves according to Eq. (4). For compressible flows, the algebraic relationships for the parameters in Eq. (7) additionally depend on the Mach number at the boundary-layer edge. Also for compressible flows, as above for the TS database, the incompressible shape parameter is used. The compressible shape parameter is not useful here because, for example, its value at separation varies strongly with the Mach number. In could be shown that this simplified approach yields good approximations for the spatial growth rates of Tollmien–Schlichting waves, not only for Falkner–Skan solutions, but for a wide range of boundary-layer flows [28].

The simplified approach for crossflow instabilities is a modification of the two-dimensional approach for inflectional instabilities and uses Stuart's theorem that states that for the temporal theory and incompressible flow the solution of a three-dimensional stability problem can be reduced to an equivalent two-dimensional stability problem. This reduction is achieved by the projection of the steady and parallel mean velocity vector $\boldsymbol{v} = U(y)\boldsymbol{e}_{x'} + W(y)\boldsymbol{e}_{z'}$ in the propagation direction of the disturbance wave characterized by the wave propagation angle Ψ relative to the external streamline and the wave number vector $\boldsymbol{k} = \alpha\boldsymbol{e}_{x'} + \beta\boldsymbol{e}_{z'}$ based on a sinusoidal disturbance of the form

$$\boldsymbol{v}' = \boldsymbol{v}_0'(y)E^{i(\alpha x' + \beta z' - \omega t)} = \boldsymbol{v}_0'(y)E^{(\omega_i t)}E^{i(\alpha x' + \beta z' - \omega_r t)} \tag{8}$$

with $\Psi = \arctan(\beta/\alpha)$, $\omega = \omega_r + i\omega_i$, and $\omega_r = 2\pi f$. Here $\boldsymbol{e}_{x'}$ denotes the external streamline direction and $\boldsymbol{e}_{z'}$ the second tangential direction perpendicular to $\boldsymbol{e}_{x'}$. The projected velocity profile $U_\Psi(y)$ reads

$$U_\Psi(y) = \frac{\alpha}{\sqrt{\alpha^2+\beta^2}}U(y) + \frac{\beta}{\sqrt{\alpha^2+\beta^2}}W(y) \tag{9}$$

and according to Stuart's theorem, the temporal stability properties of the two-dimesional $U_\Psi(y)$-profile are identical to the temporal stability properties of the real three-dimensional boundary-layer profile. To keep the spatial theory for which the two-dimensional approach has been developed, Gaster's relation is applied. This relation gives an estimation of the spatial growth rate knowing the temporal amplification rate

$$\alpha_i \approx -\omega_i/\|\boldsymbol{v}_g\| \tag{10}$$

with the spatial growth rate $-\alpha_i$, the temporal amplification rate ω_i, and the norm $\|\boldsymbol{v}_g\|$ of the group velocity vector $\boldsymbol{v}_g$ defined by

$$\boldsymbol{v}_g = \frac{\partial\omega_r}{\partial\alpha}\boldsymbol{e}_{x'} + \frac{\partial\omega_r}{\partial\beta}\boldsymbol{e}_{z'} \tag{11}$$

which represents the velocity at which energy propagates in conservative systems. The group velocity vector has an angle

$$\Psi_g = \arctan\left(\frac{\partial\omega_r/\partial\beta}{\partial\omega_r/\partial\alpha}\right)$$

with respect to the external streamline. With an extension of Gaster's relation, it is possible to estimate a spatial growth rate in an arbitrary direction denoted by the angle φ relative to the external streamline

$$\alpha_i = \frac{-\omega_i}{\|\boldsymbol{v}_g\|\cos(\varphi - \Psi_g)} \tag{12}$$

Evaluating this expression first for the chordwise direction $\boldsymbol{e}_x$ with $\varphi = -\Theta$, where Θ is the angle between the external streamline and the chordwise direction $\boldsymbol{e}_x$, leads to $\alpha_i|_{\boldsymbol{e}_x} = -\omega_i/\|\boldsymbol{v}_g\|[\cos(\Theta + \Psi_g)]^{-1}$. Next, the expression is evaluated for the direction of the wave number vector $\boldsymbol{k}$ with $\varphi = \Psi$, which is the direction of the two-dimensional $U_\Psi(y)$-profile, leading to $\alpha_i|_{\boldsymbol{k}} = -\omega_i/\|\boldsymbol{v}_g\|[\cos(\Psi - \Psi_g)]^{-1}$. With $\sigma = \alpha_i|_{\boldsymbol{e}_x}$ and $\sigma_\Psi = \alpha_i|_{\boldsymbol{k}}$ one finds an expression for the spatial growth rate in the direction of the chordwise direction $\boldsymbol{e}_x$ in terms of the spatial growth rate in the wave propagation direction denoted by Ψ

$$\sigma = \sigma_\Psi\frac{\cos(\Psi - \Psi_g)}{\cos(\Theta + \Psi_g)} \tag{13}$$

The simplification that the group velocity vector direction is more or less aligned with the external streamline yields

$$\sigma \approx \sigma_\Psi\frac{\cos(\Psi)}{\cos(\Theta)} \tag{14}$$

σ_Ψ is estimated using an extension of the method initially developed for two-dimensional basic flow, the angle Θ is given by the main flow, the wave propagation angle can be fixed as a parameter, and the growth rate σ is used for the integration of the N factor curves.

The generalization of the two-dimensional procedure uses the same two parameters as in the preceding section, but related to the inflection point of the $U_\Psi(y)$-profile 1) the mean velocity at the inflection point $(U_\Psi/U_{e,\Psi})_{\text{infl},\Psi}$, and 2) a measure for the shear stress at the inflection point

$$P_{\text{infl},\Psi} = \left[\frac{y}{\delta}\frac{d(U_\Psi(y)/U_{e,\Psi})}{d(y/\delta)}\right]_{\text{infl},\Psi}$$

and the equivalent reduced frequency $F = \omega\nu_e/U_{e,\Psi}^2$. Also in the modified approach for crossflow instabilities, simple, algebraic relationships for $Re_{\delta_i^* k}$, $k = 0$, 1, $Re_{\delta_i^* M}$, and σ_M are used. These relationships are different from those of the two-dimensional procedure and can be found in [9]. The coefficients of these relationships have been determined by exact three-dimensional stability computations. For compressible flows, the inflection point of the velocity profile is determined using the condition $\partial/\partial y(\rho\partial U_\psi/\partial y) = 0$ instead of $\partial^2 U_\psi/\partial y^2 = 0$ and the inflection point parameter is multiplied by the density value at the inflection point

$$P_{\text{infl},\Psi} = \left[\rho(y)\frac{y}{\delta}\frac{d(U_\Psi(y)/U_{e,\Psi})}{d(y/\delta)}\right]_{\text{infl},\Psi}$$

The two e^N-database methods are applied using the two N factor method [30–33] using the N factor for Tollmien–Schlichting waves $N|_{x^T}^{\text{TS}}$ and the N factor for crossflow waves $N|_{x^T}^{\text{CF}}$.

For the modeling of transitional flow regions, the intermittency function of Dhawan and Narasimha [34] is used in the same way as it was done in [35]. The extent of the transitional region is determined using algebraic transition length models according to Walker [36]. The formulas given in [36] are applied in a representation for flows with pressure gradient when a transition point is determined by one of the e^N-database methods or in a modified form as in [18] when a transition point is approximated by a laminar separation point from the boundary-layer code. When transition is fixed at a laminar separation point from the RANS code during the transient phase of the computation, a representation of the formulas for flows without pressure gradient is used. Details are given in [18,19,37]. The formulas for the modeling of transitional flow are applied to the wing sections for which transition prediction is to be performed. These wing sections have to be specified by the code user before the computation is started. The transition points on the upper and lower sides of the wing sections represent the transition line in the form of a

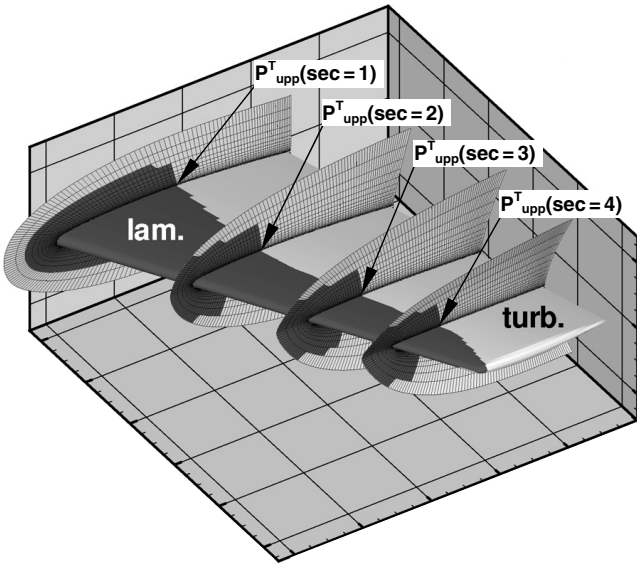

Fig. 2 Laminar zone on a wing surface.

polygonal line. For surface grid points which are located between two wing sections, the values of the intermittency function are determined via linear interpolation in spanwise direction. After all of the surface points on upper and lower sides of a wing section have been assigned to either the corresponding laminar, turbulent, or transitional interval, the field points, all points apart from the solid walls, are treated in the following way [16]. Within a limiting wall normal distance that can be adjusted by the user of the code, every field point assumes the status of the surface point that is located nearest to the field point. By this treatment, a laminar and a transitional zone for the wing are generated within the turbulent remainder of the computational grid. A partitioning into a pure laminar zone within the turbulent remainder of the flow domain (point transition) is shown in Fig. 2.

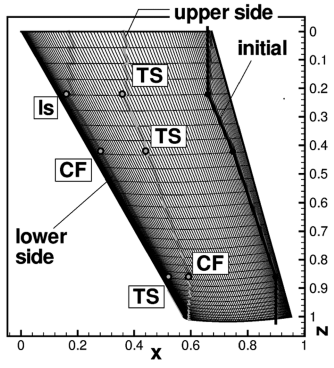

a) Initial and predicted transition lines

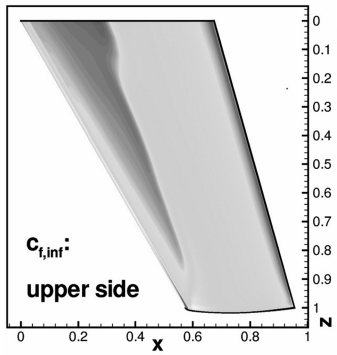

b) Skin friction distribution on upper side

Fig. 3 ONERA M6 wing.

III. Computations

A. Results

The automated transition prediction functionality of the coupled system was investigated using a number of different settings of the aerodynamic parameters for the ONERA M6 wing [38]. The ONERA M6 wing is a single element semispan swept, tapered wing with an aspect ratio $A = 3.8$ and a taper ratio $\lambda = 0.562$. The leading edge sweep angle is $\Lambda_{\mathrm{LE}} = 30$ deg, the trailing edge sweep angle is $\Lambda_{\mathrm{TE}} = 15.8$ deg, leading to a sweep angle of 26.7 deg at the 25% line of the wing. It uses a symmetric airfoil using the ONERA D section perpendicularly to the 40% line. The wing was designed to be used for studies of three-dimensional flows from low to transonic speeds at high Reynolds numbers.

In Fig. 3, the results of a preliminary test computation using a block-structured grid with about 384,000 grid points is shown. The grid has 176 cells in circumferential direction from the trailing edge on the lower side of the wing around the nose and back to the trailing edge on the upper side, and 32 cells in spanwise direction from the wing root to the wing tip. From the wing surface to the far-field edge of the grid, 48 cells are distributed. For $M_\infty = 0.84$, $Re_\infty = 2.0 \times 10^6$ (based on the mean aerodynamic chord of the wing $c_m = 0.64607$), and $\alpha = -4.0$ deg using the Baldwin–Lomax turbulence model [39], the principal functioning of the procedure was demonstrated. The limiting N-factors $N|_{x^T}^{\mathrm{TS}} = 4.0$ and $N|_{x^T}^{\mathrm{CF}} = 2.0$ were arbitrarily chosen to show how the different transition mechanisms which are presently covered by the transition prediction module (Tollmien–Schlichting waves, crossflow instabilities, and transition due to laminar separation) occur in one test case and are detected by the transition prediction module. The preceding depiction shows the initial and the predicted transition lines on the upper and the lower sides of the wing. The transition points were predicted in three different wing sections. The character of the transition mechanism is marked with TS for Tollmien–Schlichting wave, with CF for crossflow instability, and with ls for transition due to a laminar separation. Here, the transition lines were extrapolated with constant values from the transition points which are located nearest to the wing root and the wing tip beyond the wing root and the wing tip. The following depiction shows the skin friction distribution c_f on the upper side of the wing. The transition region is clearly visible by the strong rise of the skin friction downstream of the transition line.

For the next test case, the aerodynamic parameters were set according to [38], $M_\infty = 0.8395$ and $Re_\infty = 11.72 \times 10^6$, to compare the computational pressure distributions with experimental ones for $\alpha = 3.06$ deg given in the same reference. This test case is a classic CFD validation case and has become a standard for CFD codes. The measurements documented in [38] were performed with free transition in the ONERA S2MA (Modane Center) wind tunnel for which a turbulence intensity of $Tu = 0.2\%$ is given. Using Mack's relationship for the two N factors, $N|_{x^T}^{\mathrm{TS}} = N|_{x^T}^{\mathrm{CF}} = 6.485$ was applied. The case was computed using the algebraic Baldwin–Lomax (BL) turbulence model, the Spalart–Allmaras one-equation model [40] with Edwards and Chandra modification [41] (Spalart–Allmaras–Edwards = SAE), and the Wilcox k–ω two-equation turbulence model [42].

In Fig. 4, a comparison of the computed and the experimental c_p-distributions is shown for the nondimensional spanwise wing sections $\eta = z/b = 0.2$, 0.44, 0.65, 0.8, 0.9, 0.95, and 0.99. The computational results for the three different turbulence models differ only very weakly from one another. There are some deviations of the computed c_p-distributions from the experimental ones in the two first wing sections from the wing root, $\eta = 0.2$ and 0.44, due to the wall influence in the experiment. In the experiment, the wing was elongated by a spacer which was mounted to the wind tunnel wall. Between the spacer and the wing, an end plate which resembles a boundary-layer fence was situated. This arrangement leads to a flow which is far from being symmetric with respect to the spanwise direction. In the computations, however, a symmetry boundary condition in spanwise direction was applied. In wing section $\eta = 0.8$, one can still see the two shocks of the lambda shock system although

the reexpansion downstream of the first shock is not captured. In sections $\eta = 0.9$, and 0.95, the shock strength and the reexpansion after the, from now on, single shock is reproduced best by the SAE turbulence model. The agreement of the computed and experimental c_p-distributions, apart from the wing root and the trailing-edge region of the wing tip, is of good quality.

In Fig. 5, the surface pressure distributions, the skin friction lines, and the transition lines for the three cases are shown. The lambda shock system is clearly visible. The transition lines which are marked as dashed-dotted white lines are located very near the leading edge on the upper and lower side of the wing and are almost identical for the three cases. The transition locations were predicted for three wing sections ($\eta = 0.22$, $\eta = 0.42$, and $\eta = 0.86$) on the upper and lower sides of each section. As can be seen, the transition lines run along a constant local chordwise position over wide portions of the wing. All transition points occurred due to crossflow instabilities.

The computations using the Baldwin–Lomax and SAE turbulence models predict a flow separation point directly downstream of the shock at the wing section $\eta \approx 0.92$ where the skin friction line pattern exhibits a saddle point [43].

Computational results obtained for another computational grid with about 800,000 grid points can be found in [37]. There, some minor differences in the c_p-distributions and the skin friction lines occur due to the different cell densities and the distribution of the grid points. The predicted transition lines, however, are almost identical.

The next test case is based on the experiments reported in [44] where the ONERA M6 wing was investigated for $M_\infty = 0.262$ and $Re_\infty = 3.5 \times 10^6$ in the ONERA S2Ch (Chalais–Meudon) wind tunnel for which again a turbulence intensity of $Tu = 0.2\%$ is given. In the experiments, the laminar regions were detected and visualized applying a sublimation technique based on naphthalene. The laminar regions are documented as reprints of photographs for the angles of attack $\alpha = 0, 5$, and 15 deg for the upper and lowers sides of the wing. For the wing section $\eta = 0.45$, the development of the transition points on upper and lower sides is given in a diagram for $\alpha = 0, 5, 10$, and 15 deg. Using again Mack's relationship for the two N factors, $N|_{x^T}^{\mathrm{TS}} = N|_{x^T}^{\mathrm{CF}} = 6.485$, the cases were computed using the SAE turbulence model. The transition locations were predicted for three wing sections ($\eta = 0.22$, $\eta = 0.42$, and $\eta = 0.86$) on the upper and lower sides of each section, where $\eta = 0.42$ corresponds to the grid line nearest to $\eta = 0.45$, the section for which most experimental transition information is available for this test case.

The experimental results of the transition detection from [44] are depicted in Fig. 6 and give an impression of the extent and the shape of the laminar regions for $\alpha = 0$, 5, and 15 deg.

In Fig. 7, the computed transition lines for the same angles of attack are depicted. A comparison of the measured laminar regions and the computed transition lines exhibits a number of deviations. Some of these deviations can be explained easily, others can not. The deviations at the wing root and the wing tip are due to the way the initial transition lines were defined for these calculations. At the root, the starting points of the transition lines on the upper and lower sides are located outside the computational grid, i.e., their spanwise coordinates are negative, and their chordwise coordinates are lower than the minimum x-coordinate of the wing root section in the symmetry plane. By this setting of the starting point of a transition line, the laminar region in the computational grid, which is created basically by a mapping procedure of a polygonal line representing the current transition line into the surface grid [16], near the wing root is forced to be small or it does not exist at all. This is usually the case when the wing is mounted to an aircraft fuselage or to a wind tunnel wall, where the turbulent boundary layers from the fuselage or the wall prevent laminar flow over the wing in the region of the wing–body junction or the wing–wall junction. Apparently, the fencelike end plate between the wing and the spacer has not affected the flow in such a way. At the tip, the situation for the ending points of the transition lines is similar as just described. The ending points of the transition lines on the upper and lower sides are located upstream of the minimum chordwise coordinate of the wing tip and very slightly beyond the wing tip with respect to the spanwise direction. Thus, at the wing tip itself the flow is always fully turbulent and even a spanwise portion of the outboard wing may be forced to be fully turbulent depending on the running of the current transition line as can be seen in the results for $\alpha = 0$ and 15 deg. These deviations can be eliminated immediately through a change of the starting point and ending point positions, or when the first and last wing sections used in the transition prediction loop are chosen such that they are located near enough to the wing root and the wing tip, which is only a matter of a new setting of the input parameters for the transition prediction iteration.

The transition lines on the wing upper side for $\alpha = 5$ and 15 deg and on the lower side for $\alpha = 15$ deg seem to be of good accuracy. Whereas the two upper side transition lines are due to laminar separations in all wing sections where transition was predicted, the lower side transition line for $\alpha = 15$ deg is completely due to crossflow instabilities. It seems that the upper side transition line for $\alpha = 15$ deg from the experiment is located slightly downstream of the upper side transition line for $\alpha = 5$ deg, whereas the simulations yield the opposite tendency. For $\alpha = 0$ deg, the transition lines on both sides, (all transition points are due to laminar separations) are located 50% too far upstream compared with the experiment. For all these cases where the transition points were approximated by laminar separation points from the boundary-layer code, it can happen that the approximation is not good enough depending on the extent of a laminar separation bubble which must have existed in the experiment. Here, it seems necessary to apply an empirical or semi-empirical criterion [45] for the prediction of the transition point inside the laminar separation bubble.

It must be emphasized that the computed transition lines on upper and lower sides for $\alpha = 0$ deg are exactly symmetric with respect to the numerical values in the wing sections where transition was predicted, whereas the laminar regions from [44] depicted in Fig. 6 are not. Here, it must be asked if this asymmetry is an optical effect due to a reception problem during the recording of the images in the experiment or a problem during the reproduction of the images on the one hand, or if effectively a flow asymmetry existed during the experiment on the other hand. If the latter should be the case, some of the deviations can be explained by this asymmetry.

Moreover, it must be noticed that in all depictions from the experiment, the laminar regions exhibit a deformation in the inboard wing region at a spanwise station of $\eta \approx 0.25$ towards the wing leading edge. This deformation is pronounced strongest on the upper side for $\alpha = 5$ and 15 deg and on the lower side for $\alpha = 0$ and 15 deg, and still clearly visible on the upper side for $\alpha = 0$ deg. A clear statement for the lower side for $\alpha = 5$ deg cannot be made, although the strong distortion of the rear part of the laminar region at a similar spanwise station may be a sign of the same effect. The knowledge of the reason for this deformation definitely helps to understand the deviations between experiment and simulation.

Additionally, for the lower side at $\alpha = 5$ deg, the depiction of the laminar region exhibits large black areas near the leading edge inside white surroundings. For all the other depictions, the distinction between laminar regions in white and turbulent regions in black can be made relatively clearly and easily. The interpretation for the lower side for $\alpha = 5$ deg is not as easy. Here, it is necessary to know whether the naphthalene did not completely sublimate when the image was taken, whether it was not properly coated to the surface in these regions of the wing, or whether an optical effect as previously described is responsible for this uncertainty. If the latter should be the case, it is necessary to know where in all the other depictions this optical effect might have played a role to do a proper comparison between computation and experiment.

Significant is the large chordwise extent of the laminar region on the lower side of the inboard wing region for $\alpha = 5$ deg. The simulation tends to reproduce this behavior well. The spanwise extent of the laminar region in the computation can be improved significantly if the computed transition line is calculated at more than only three wing sections, using enough wing sections in the region to be considered.

A deviation between experimental and computed results, which cannot be explained easily, is the fact that the computed transition

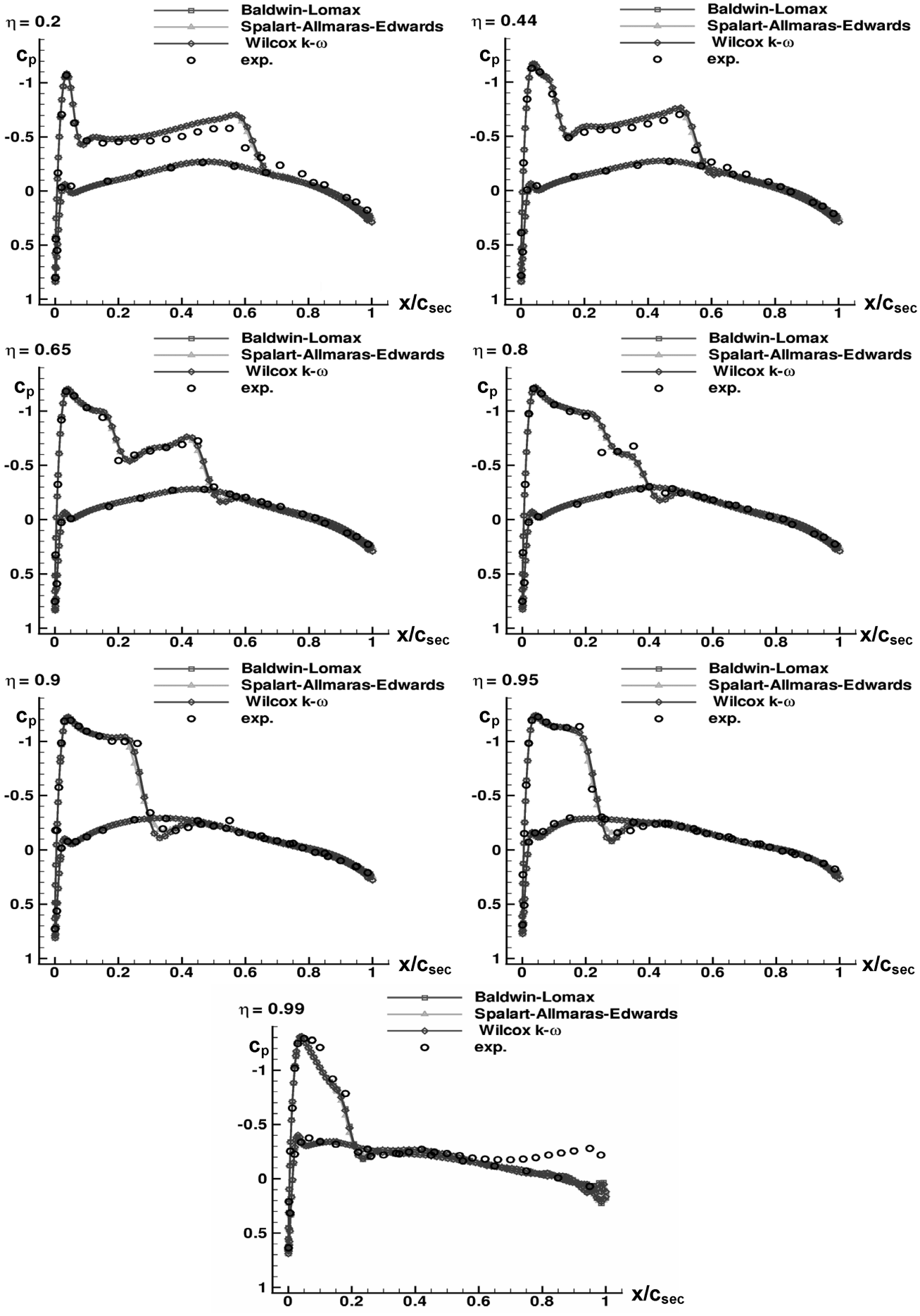

Fig. 4 Measured and computed c_p-distributions, M6 wing, three turbulence models.

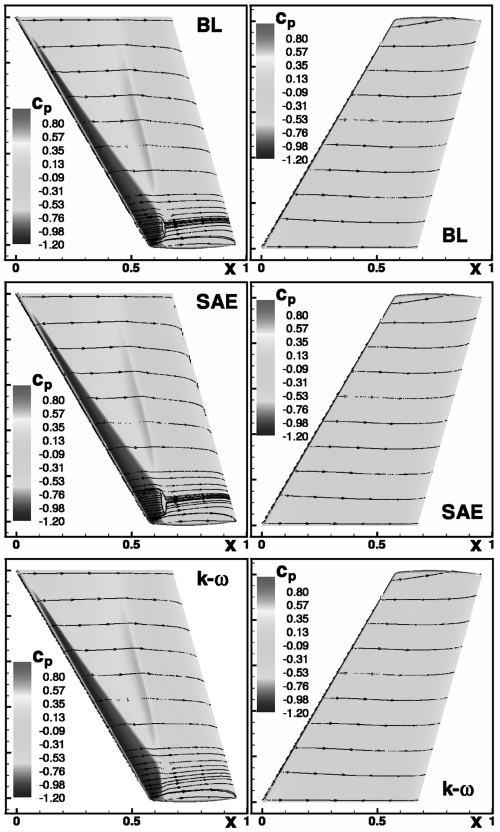

Fig. 5 Surface c_p-distributions, skin friction lines, and transition lines, three different turbulence models.

line on the lower side for $\alpha = 5$ deg is located too far downstream over the whole span compared with the depiction in Fig. 6. The transition points are due to a crossflow instability in section $\eta = 0.42$ and due to Tollmien–Schlichting instabilities in sections $\eta = 0.22$ and $\eta = 0.86$.

In Fig. 8, the experimental transition locations on the upper and lower sides in wing section $\eta = 0.45$ for $\alpha = 0$, 5, 10, and 15 deg as they are given in [44] are depicted and compared with those from the computations in section $\eta = 0.42$. Additionally, for $\alpha = 5$ deg, the predicted values from supplementary computations where the Baldwin–Lomax turbulence model was applied for comparison purposes are plotted. On the one hand, the comparison illustrates the dimension of the deviations which are clearly not acceptable for $\alpha = 5$ deg on the wing lower side. On the other hand, it shows that the transition prediction procedure does not depend on the turbulence model used. The numerical values of the predicted transition locations are almost identical. The same circumstance is illustrated in Fig. 9 where Secs. 1, 2, and 3 correspond to the wing sections

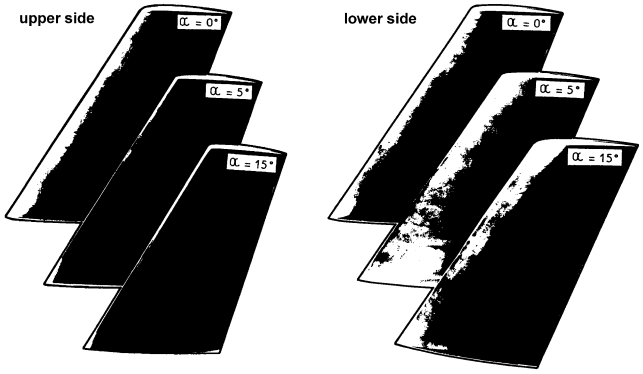

Fig. 6 Measured laminar regions on the M6 wing for $M_\infty = 0.262$ and $Re_\infty = 3.5 \times 10^6$.

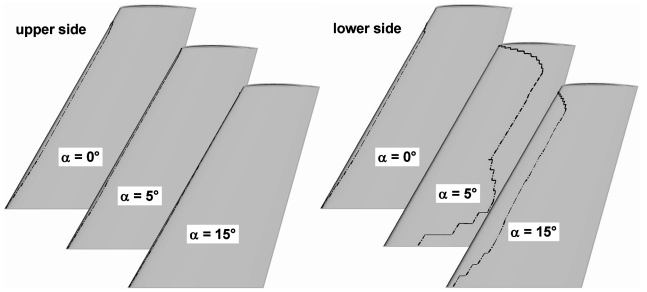

Fig. 7 Computed transition lines on the M6 wing, $N|_{x_T}^{\mathrm{TS}} = N|_{x_T}^{\mathrm{CF}} = 6.485$.

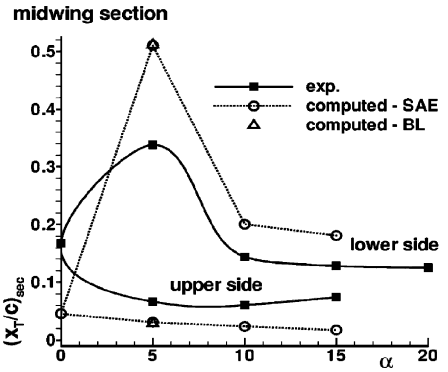

Fig. 8 Computed transition points in the midwing section of the M6 wing, $N|_{x_T}^{\mathrm{TS}} = N|_{x_T}^{\mathrm{CF}} = 6.485$.

$\eta = 0.22$, $\eta = 0.42$, and $\eta = 0.86$. Here, the maximum N factor curves at the end of the transition location iteration yielded by the two e^N-database methods for the lower sides of the three different wing sections, based on the computations using the two different turbulence models, are depicted. There is almost no difference due to the use of the different turbulence models for Tollmien–Schlichting as well as for crossflow waves. The curves of the N factors for Tollmien–Schlichting waves are very close to each other, although Sec. 1 is an inboard wing section, Sec. 2 is a midboard wing section, and Sec. 3 is an outboard wing section. In Secs. 1 and 3, the N factors for crossflow waves are very close to each other and do not meet the critical N factor $N_{\mathrm{crit}} = N|_{x_T}^{\mathrm{TS}} = N|_{x_T}^{\mathrm{CF}} = 6.485$ in the area where the experimental transition point was detected. The N factors for Sec. 2 are significantly higher than those of the other two sections and meet the critical N factor at $(x/c)_s \approx 0.51$ of wing section $\eta = 0.42$. From the very different running of the curves for TS waves on the one hand and CF waves on the other hand, it seems to be evident that transition in all sections must have occurred due to crossflow instabilities, not due to Tollmien–Schlichting instabilities. To find out the reason for these deviations, a number of comparisons for the midboard wing section $\eta = 0.42$ were carried out using the Baldwin–Lomax turbulence model.

B. Effective Sweep Angle

A possible influencing variable is the effective sweep angle. The effective sweep angle [46] represents the impact of a number of geometrical parameters of an aircraft or of a wing configuration, which influence the flowfield and cause additional velocity components by three-dimensional displacement effects and thus increase the velocity of the flow along the wing leading edge. Some of these geometrical parameters are, for example, the wing itself, the fuselage, and the engine nacelle. Others are, for example, the aspect ratio and the taper ratio of the wing, the wing sweep, and the absolute wing thickness ratio. The absolute wing thickness ratio has the most significant effect as it was shown in [46]. The effective sweep angle is defined in [46] as

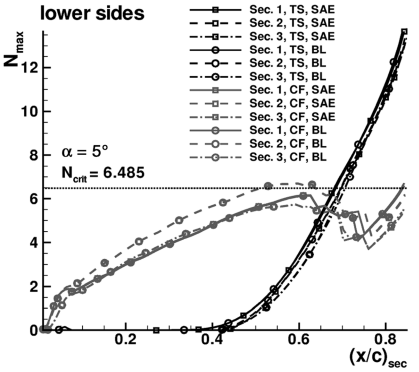

Fig. 9 *N* **factor curves of TS and CF waves of the ONERA M6 wing.**

$$\Lambda_{\text{eff}} = \Lambda_{\text{LE}} + \Delta\Lambda = \arcsin(U_{e,\min}/\|\boldsymbol{v}_\infty\|) = \arcsin(U_{e,\text{AL}}/\|\boldsymbol{v}_\infty\|) \tag{15}$$

where $U_{e,\min} = U_{e,\text{AL}}$ is the tangential velocity value at the boundary-layer edge associated with the corresponding point of the attachment line. The corresponding point of the attachment line is determined by detecting the point having the maximum c_p value $c_{p,\max,s}$ in a wing section of the computational grid, and the tangential velocity value at the boundary-layer edge for the current wing section $U_{e,\text{AL,s}}$ is determined applying

$$U_{e,\text{AL,s}} = \sqrt{2\frac{\kappa}{\kappa-1}RT_\infty\left[1+\frac{\kappa-1}{2}M_\infty^2-\left(1+\frac{\kappa}{2}M_\infty^2 c_{p,\max,s}\right)^{\frac{\kappa-1}{\kappa}}\right]} \tag{16}$$

so that Λ_{eff} is determined as a local quantity $\Lambda_{\text{eff,s}}$ for each wing section. According to [46], for the ATTAS/VFW-614 aircraft of the DLR, German Aerospace Center, values of $\Delta\Lambda \approx 2$ to 3 deg were found for the midwing section $\eta = 0.45$.

The only way to account for the effective sweep angle in the transition prediction procedure presented is to communicate it to the laminar boundary-layer code which provides all viscous layer data for the e^N-database methods. In so doing, it may be necessary also to modify the c_p-distribution of the current wing section, because the boundary-layer code generates the boundary-layer edge velocity components based on the assumption of isentropic flow at the boundary-layer edge according to Eq. (16). If the c_p values from the RANS solver exceed the maximum value, which is theoretically possible in the attachment line point, the boundary-layer code stops and the computation of the viscous layer data is aborted. This situation may occur if $\Delta\Lambda$ is positive and exceeds a certain value so that $c_{p,\max,s}$ and Λ_{eff} are not compatible anymore because $c_{p,\max}(\Lambda_{\text{eff}}) < c_{p,\max}(\Lambda)$ for $\Lambda_{\text{eff}} > \Lambda$.

For testing purposes a number of different values for $\Delta\Lambda$ in the range $1.0\,\text{deg} \le \Delta\Lambda \le 3.0\,\text{deg}$ were applied and the CF *N* factor curves for the lower side of the midwing section, $\alpha = 5$ deg, of the M6 wing were computed based on the c_p-distribution obtained with the Baldwin–Lomax model. For all tests, it was necessary to reduce the c_p value in the attachment line point and it was set to the theoretical value $c_{p,\max}(\Lambda_{\text{eff}})$. For all tests with $\Delta\Lambda \ge 1.35$ deg, it was necessary to reduce also the c_p value at the second surface grid point downstream of the attachment line point because here the c_p value was greater than the theoretical value $c_{p,\max}(\Lambda_{\text{eff}})$ too. The value given to the second surface grid point was set to the average value of the theoretical value $c_{p,\max}(\Lambda_{\text{eff}})$ and the c_p value of the third surface grid point downstream of the attachment line point whose value was always well below the theoretical value $c_{p,\max}(\Lambda_{\text{eff}})$. The results obtained by these modifications are depicted in Fig. 10. All cases where the c_p values of the first two points were modified are characterized by significantly higher *N* factor values and higher slopes of the *N* factor curves. The *N* factor values and the slopes of the *N* factor curves rise with increasing values of $\Delta\Lambda$. It is obvious that the applied modifications significantly influence the *N* factor results in an unacceptable way. It was found that the same undesired effect is produced for $\Delta\Lambda = 1.0$ and $\Delta\Lambda = 1.25$ deg when the c_p value of the second surface grid point downstream of the attachment line point is modified in the same way as for $\Delta\Lambda \ge 1.35$ deg. The same effect occurs when the c_p value of the second surface grid point is determined by linear interpolation and even if $\Delta\Lambda = 0.0$ deg is applied and the c_p value of the second surface grid point downstream of the attachment line point is modified. Not until a c_p value of $c_p \approx 0.7405$ is applied at the second surface grid point, so that the convexity of the c_p curve has increased up to a certain extent, the original *N* factor curve is reproduced almost exactly. Increasing the c_p value at the second surface grid point, and thus increasing the convexity of the c_p curve more and more up to a c_p value so that the boundary-layer code detects a laminar separation at the second surface grid point, leads to a strong decrease of the values of the *N* factors without significantly influencing the slope of the *N* factor curve [37]. Finally, it can be concluded that a modification of only those c_p values which exceed the theoretical value $c_{p,\max}(\Lambda_{\text{eff}})$ can lead to an uncontrolled change of the values and the slope of the *N* factor curve, and thus hides the effect of the effective sweep angle and is considered an inappropriate way of a modifying the c_p-distribution.

In Fig. 11, two different modifications of the c_p-distribution which seem to be appropriate and the results in terms of the CF *N* factor curves are depicted. Modification 1 is based on the difference between the computed maximum c_p value $c_{p,\max,s}$ and the theoretical value $c_{p,\max}(\Lambda_{\text{eff}})$ with $\Delta c_p^{(1)} = c_{p,\max,s} - c_{p,\max}(\Lambda_{\text{eff}})$. The complete c_p-distribution is then altered by $c_p^{(1)}(P_S) = c_p(P_S) - \Delta c_p^{(1)}$ for all surface grid points P_S of the current side of the wing section. Thus, a constant positive shift of the c_p-distribution is caused, whereas the shape of the c_p-distribution is exactly preserved. Modification 2 is based on the percentage difference between the computed maximum c_p value $c_{p,\max,s}$ and the theoretical value $c_{p,\max}(\Lambda_{\text{eff}})$ so that $c_p^{(2)}(P_S) = c_p(P_S)[c_{p,\max}(\Lambda_{\text{eff}})/c_{p,\max,s}]$ for all surface grid points P_S of the current side of the wing section. Thus, a

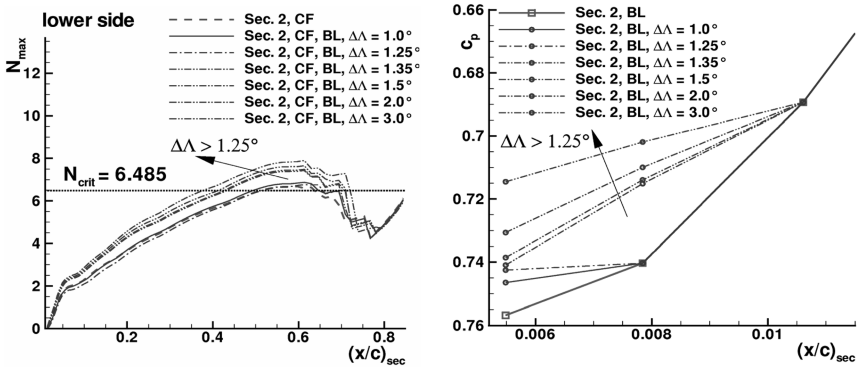

Fig. 10 *N* **factor curves of CF waves and modified c_p-distributions.**

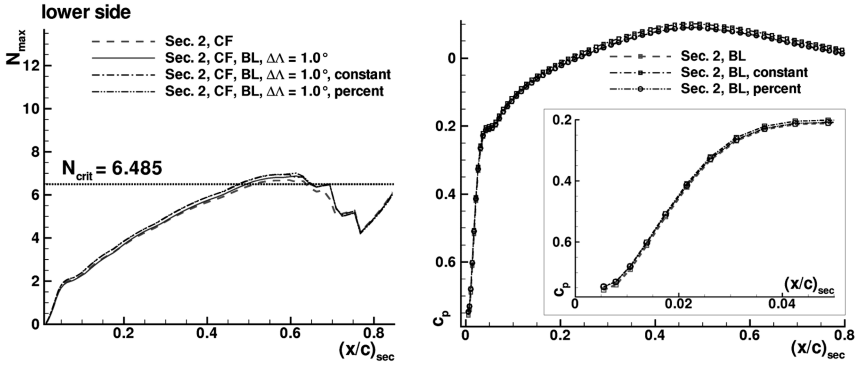

Fig. 11 N factor curves of CF waves and different modified c_p-distributions ($\alpha = 5\,\mathrm{deg}$).

slight positive shift and a smooth change of the shape of the c_p-distribution are caused directly downstream of the attachment line point, and only a negligible change of the c_p values and of the shape is caused along the rest of the c_p-distribution. In the FLOWer code, modification 2 is applied.

The two modifications were applied for $\Delta\Lambda = 1.0\,\mathrm{deg}$ and Fig. 11 shows that for the investigated case, the results in terms of the N factor curves based on the two modifications are almost identical. The values of the N factors and the slope of the N factor curves are slightly higher than those of the unmodified c_p-distribution. For comparison purposes, the N factor curve for the c_p-distribution with solely a reduced c_p value in the attachment line point from Fig. 10 is plotted. The differences between the curves are clearly visible but do not have a significant effect with respect to the transition location.

Based on Eq. (15), the values for $\Delta\Lambda$ for the three wing sections where the transition locations were predicted are in the range $0.65\,\mathrm{deg} \leq \Delta\Lambda \leq 1.24\,\mathrm{deg}$. The corresponding effective sweep angles do not lead to considerable improvements of the transition locations in all sections. A formula for the effective sweep angle which yields slightly different values can be derived from the view depicted in Fig. 12. With $v_n = v_\infty \cos(\Lambda_{\mathrm{LE}})\Lambda$, $v_t = v_\infty \sin(\Lambda_{\mathrm{LE}})$, $v_{t,\mathrm{eff}} = v_t + \Delta v_t = v_t^{\mathrm{code}}$, and $\tilde{v}_\infty^2 = v_n^2 + v_{t,\mathrm{eff}}^2$ one obtains

$$\Lambda_{\mathrm{eff}} = \Lambda_{\mathrm{LE}} + \Delta\Lambda = \arctan\left(\frac{v_{t,\mathrm{eff}}}{v_\infty \cos(\Lambda_{\mathrm{LE}})}\right) \tag{17}$$

with $v_{t,\mathrm{eff}} = U_{e,\min} = U_{e,\mathrm{AL}} = U_{e,\mathrm{AL,s}}$. Based on Eq. (17), the values for $\Delta\Lambda$ for the three wing sections where the transition locations were predicted are in the range $0.49\,\mathrm{deg} \leq \Delta\Lambda \leq 0.91\,\mathrm{deg}$, so that the impact of the effective sweep angle is even lower than before. In all the tests which were made for the investigation of the influence of the effective sweep angle, the effect of all modifications of the c_p-distributions and the effective sweep angle itself had only a negligible or even no impact on the maximum N factor curves of the Tollmien–Schlichting waves.

C. Stability Boundary

The application of the two N factor method using the critical N factor for Tollmien–Schlichting waves $N|_{x^T}^{\mathrm{TS}}$ and the critical N factor for crossflow waves $N|_{x^T}^{\mathrm{CF}}$ requires two different numerical values for $N|_{x^T}^{\mathrm{TS}}$ and $N|_{x^T}^{\mathrm{CF}}$. The case $N_{\mathrm{crit}} = N|_{x^T}^{\mathrm{TS}} = N|_{x^T}^{\mathrm{CF}}$ is a special case, and Mack's relationship which can be applied with some confidence for wind tunnel conditions is strictly valid only for streamwise instabilities.

In [47], different values for $N|_{x^T}^{\mathrm{TS}}$ and $N|_{x^T}^{\mathrm{CF}}$ for the ONERA S2Ch wind tunnel are applied. The numerical values $N_{\mathrm{crit}}^{\mathrm{TS}} = N|_{x^T}^{\mathrm{TS}} = 7.0$ for TS dominated transition and $N_{\mathrm{crit}}^{\mathrm{CF}} = N|_{x^T}^{\mathrm{CF}} = 6.0$ for CF dominated transition are based on a very limited number of experimental data for infinite swept wing tests, which were made for a model equipped with the ONERA D airfoil at two different Reynolds numbers, $Re_\infty = 1.0 \times 10^6$ and $Re_\infty = 1.5 \times 10^6$. The stability limit for mixed (TS and CF dominated) transition is approximated by a linear curve as shown in Fig. 13a by the "stability boundary No. 1." In this

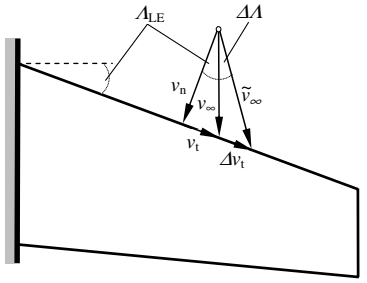

Fig. 12 Effective sweep angle.

approximation, the limit for TS dominated transition is defined by the point $[N^{\mathrm{CF}}, N^{\mathrm{TS}}]_{\mathrm{TS,lim}} = [3.5, 7.0] = [3.5, N_{\mathrm{crit}}^{\mathrm{TS}}]$ and the limit for CF dominated transition is defined by the point $[N^{\mathrm{CF}}, N^{\mathrm{TS}}]_{\mathrm{CF,lim}} = [6.0, 5.5] = [N_{\mathrm{crit}}^{\mathrm{CF}}, 5.5]$. These four coordinates in the $N_{\mathrm{crit}}^{\mathrm{CF}} - N_{\mathrm{crit}}^{\mathrm{TS}}$ plane and the curve which approximates the stability limit for mixed transition are degrees of freedom for the determination of the stability boundary. The fixing of the four coordinates in the $N_{\mathrm{crit}}^{\mathrm{CF}} - N_{\mathrm{crit}}^{\mathrm{TS}}$ plane are a crucial point and a sufficient number of measured points in the $N_{\mathrm{crit}}^{\mathrm{CF}} - N_{\mathrm{crit}}^{\mathrm{TS}}$ plane must be available to obtain a reliable approximation of the stability boundary.

The approximation of the stability limit for mixed transition in the FLOWer code is done using a quarter of an ellipse. Using the same values for $[N^{\mathrm{CF}}, N^{\mathrm{TS}}]_{\mathrm{TS,lim}}$ and $[N^{\mathrm{CF}}, N^{\mathrm{TS}}]_{\mathrm{CF,lim}}$ as in [47] yields the stability boundary No. 2 in Fig. 13a. In Fig. 13b, it is shown how the stability boundary No. 2 changes if the critical N factor for Tollmien–Schlichting waves $N_{\mathrm{crit}}^{\mathrm{TS}} = N|_{x^T}^{\mathrm{TS}} = 6.485$ based on Mack's relationship is used, instead of the value 7.0 keeping all other values as in [47] so that $[N^{\mathrm{CF}}, N^{\mathrm{TS}}]_{\mathrm{TS,lim}} = [3.5, 6.485]$ and $[N^{\mathrm{CF}}, N^{\mathrm{TS}}]_{\mathrm{CF,lim}} = [6.0, 5.5]$. Neglecting the measured point $[N^{\mathrm{CF}}, N^{\mathrm{TS}}] \approx [7.0, 2.0]$ for the high Reynolds number $Re_\infty = 1.5 \times 10^6$, assuming that the corresponding transition location was determined without sufficient accuracy, so that the related N factors are not useful leads to the stability boundary No. 2 in Fig. 13c where $N_{\mathrm{crit}}^{\mathrm{TS}} = N|_{x^T}^{\mathrm{TS}} = 6.485$, $N_{\mathrm{crit}}^{\mathrm{CF}} = N|_{x^T}^{\mathrm{CF}} = 5.75$, $[N^{\mathrm{CF}}, N^{\mathrm{TS}}]_{\mathrm{TS,lim}} = [3.5, 6.485]$, and $[N^{\mathrm{CF}}, N^{\mathrm{TS}}]_{\mathrm{CF,lim}} = [5.75, 5.0]$. All these approximations are based upon assumptions which had to be made due to the very limited number of experimental data and reveal the uncertainty which arises when too limited information is available for the determination of the stability boundary.

Figure 14 shows the three different stability boundaries No. 2 from Fig. 13 in one diagram and the $N^{\mathrm{TS}} - N^{\mathrm{CF}}$ curve of the M6 midwing section for $\alpha = 5\,\mathrm{deg}$, $M_\infty = 0.262$, and $Re_\infty = 3.5 \times 10^6$ plotted depending on the parameter $(x/c)_{\mathrm{s}}$. One can see clearly that transition in this case is strictly CF dominated. Additionally, the $(x/c)_{\mathrm{s}}$-over-N^{CF} curve is plotted for this wing section to determine that value of the N factor $N_{\mathrm{crit}}^{\mathrm{CF}} = N|_{x^T}^{\mathrm{CF}}$ which corresponds to the experimentally determined transition location located at $(x/c)_{\mathrm{s}} = 0.338$. The corresponding value is $N|_{x^T}^{\mathrm{CF}} = 5.157$ and the related stability boundary (stability boundary, current) is also depicted in Fig. 14. This CF N factor value for this side of this wing section of this one flow case is used now as calibration value for the

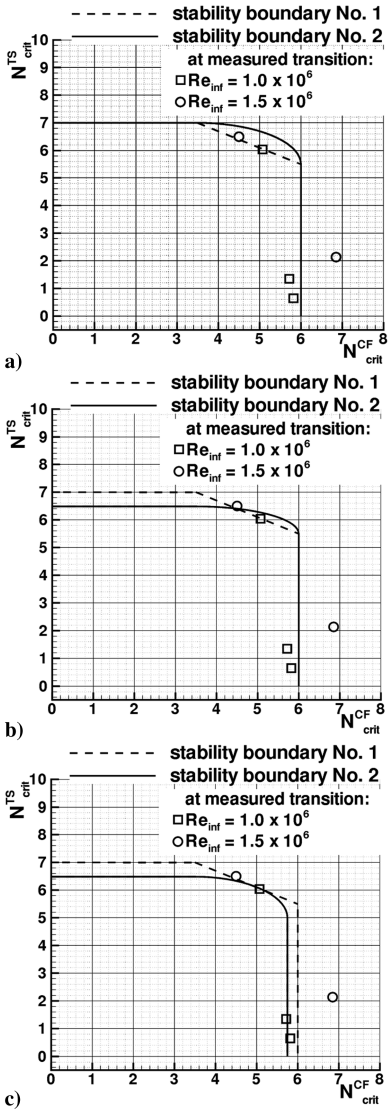

Fig. 13 Different possible stability boundaries for the ONERA S2Ch wind tunnel.

critical N factor for crossflow waves in the two N factor method because the experimental data currently available are too limited to do an estimate on an experimental basis on the one hand. On the other hand, it is evident that the experimental data shown in Fig. 13 do not resolve the problem of the strong deviations between the experimental and the computed transition locations on the wing lower side. Here, one can assume that the application of the naphthalene sublimation technique has accelerated the transition.

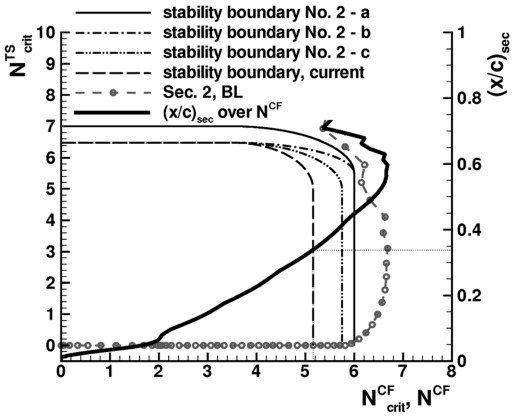

Fig. 14 Different stability boundaries, M6 midwing section.

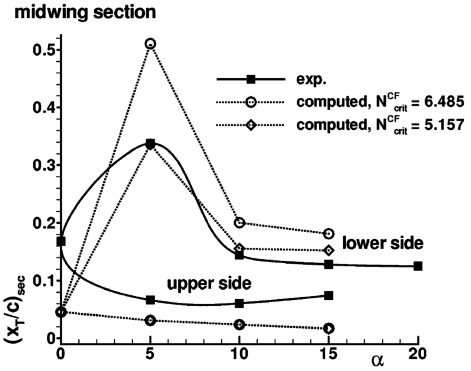

Fig. 15 Computed transition points in the midwing section of the M6 wing.

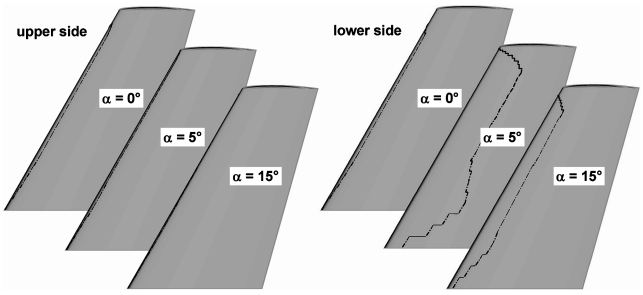

Fig. 16 Computed transition lines on the M6 wing, $N|_{x_T}^{TS} = 6.485$, $N|_{x_T}^{CF} = 5.157$, three sections.

Recomputations of all the cases which were illustrated before using the SAE turbulence model and $N|_{x_T}^{CF} = 5.157$ yield the results depicted in Fig. 15 where the computed transition points from the transition predictions with $N|_{x_T}^{CF} = 6.485$ and $N|_{x_T}^{CF} = 5.157$ are compared with the experimentally determined transition locations in the M6 midwing section. Now, for $N|_{x_T}^{CF} = 5.157$, the accuracy of the predicted transition locations on the lower side of the wing section is good. The corresponding computed transition lines on upper and lower sides of the wing are depicted in Fig. 16. Although the results for the upper side at all incidences and for the lower side at $\alpha = 0.0$ deg are identical to those obtained before for $\alpha = 5.0$ and $\alpha = 15.0$ deg, a clear improvement of the transition lines on the lower side can be noticed. The improvement is pronounced strongest for $\alpha = 5.0$ deg.

In Fig. 17, the computed transition lines for the same cases are shown whereas the transition locations were predicted now for 11 wing sections at $\eta = 0.0$, 0.11, 0.22, 0.325, 0.42, 0.8, 0.86, 0.899, 0.93, 0.96, and 0.975 on upper and lower sides. Here, a further improvement in the wing root and wing tip regions with respect to the spanwise extent and the global shape of the laminar regions is obvious. For the lower side at $\alpha = 15.0$ deg the tendency towards more downstream located transition points at the wing root and the wing tip than in the midwing area is well captured. The same effect is

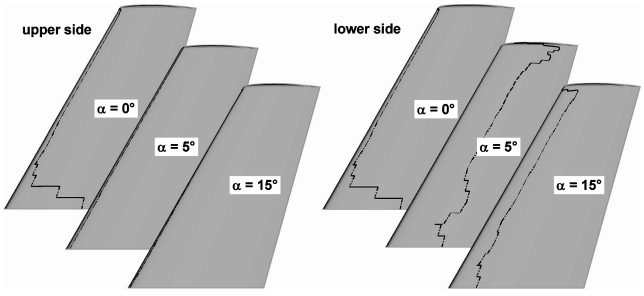

Fig. 17 Computed transition lines on the M6 wing, $N|_{x_T}^{TS} = 6.485$, $N|_{x_T}^{CF} = 5.157$, eleven sections.

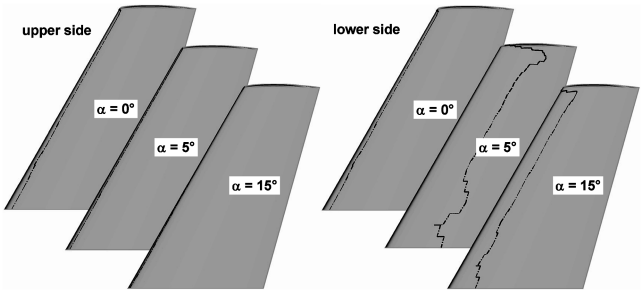

Fig. 18 Computed transition lines on the M6 wing, $N|_{x^T}^{\mathrm{TS}} = 4.75$, $N|_{x^T}^{\mathrm{CF}} = 5.157$, eleven sections.

well captured and clearly visible also for the lower side at $\alpha = 5.0$ deg although it seems that the chordwise extent of the laminar region is too small at the wing root and too large at the wing tip. It is remarkable here that transition in the three most outboard located sections at the wing tip ($\eta = 0.93$, 0.96, and 0.975) occurred due to Tollmien–Schlichting instabilities, whereas for the lower side at $\alpha = 15.0$ deg transition occurred due to crossflow instabilities at $\eta = 0.93$ and $\eta = 0.96$, and due to a laminar separation at $\eta = 0.975$. For $\alpha = 5.0$ deg, it appears as if the turbulent wedge at $\eta \approx 0.2$ on the lower side is reproduced. A better representation of the laminar region in this area of the wing with respect to its shape and its location may be obtained for a higher resolution of the computed transition line in this region in combination with a higher spanwise cell density in the computational grid. For $\alpha = 0.0$ deg, the laminar regions at the wing root deviate strongly from those detected in the experiments. In the two most inboard located sections at the wing root, $\eta = 0.0$ and $\eta = 0.11$, transition occurred due to Tollmien–Schlichting instabilities. In all other sections a laminar separation causes transition. A close inspection of the skin friction lines near the wing root exhibit that almost no crossflow velocity components exist in this region. In contrast to this finding in the result from the simulation, the end plate between the spacer and the wing root must have caused a crossflow velocity component in the experiment. It is possible that this crossflow caused transition due to crossflow instabilities. It may also be that the flow situation was such that a three-dimensional separation downstream of the leading edge occurred at the wing root in the experiment. If this was really the case, it can only be found out if the computational test case is modeled more properly, including the spacer and the end plate and maybe even including the wind tunnel wall in the computational grid. These differences in the real and the modeled geometries of this test case might be another reason for the deviations between the measured laminar regions and the computed transition lines in the wing root area. The deviations at the wing tip for the lower side at $\alpha = 5.0$ deg need a further investigation. Here, it must be clarified if the laminar regions from the experiment have in reality been as it seems in the depiction of Fig. 6 and if a direct comparison between the measured laminar regions and the computed transition lines is possible at all. It is also possible that the critical N factor for Tollmien–Schlichting instabilities must be reduced in the transition prediction procedure because it is possible that the naphthalene sublimation technique has also accelerated the TS transition. Calibrating the critical TS N factor using $N_{\mathrm{crit}}^{\mathrm{TS}} = N|_{x^T}^{\mathrm{TS}} = 4.75$ yields the results in Fig. 18 which shows a further improvement. Again, the critical N factor corresponding to the transition location of only one wing section, $\eta = 0.96$, at $\alpha = 5.0$ deg was used and applied to all other wing sections and all other angles of attack. For an assessment of this improvement, one has to take into account the experimental transition information from Figs. 6, 8, and 15. Comparing the apparent end of the laminar region on the lower side at $\alpha = 5.0$ deg in Fig. 6 and the transition location given in Figs. 8 and 15 at $\eta = 0.45$, one finds that transition occurred more downstream than Fig. 6 suggests. Assuming that this circumstance holds for the complete laminar region on the lower side at $\alpha = 5.0$ deg, the simulation yields very good results for the lower side and good results for the upper side at $\alpha = 5.0$ deg and $\alpha = 15.0$ deg with respect to the shape and chordwise extent of the computed laminar regions. For $\alpha = 0.0$ deg, the chordwise extent of the laminar regions must be enhanced applying a criterion for transition downstream of a laminar separation.

For a further validation of the transition prediction procedure, other test cases which are better suited for validation purposes must be investigated. An essential problem in this regard is to find validation test cases which provide not only the measured transition locations but also the stability boundary, or at least sufficient information to define the stability boundary with sufficient accuracy. A possible transonic test case is the flow over the DLR F5 wing which has been well documented in [48]. For free flight conditions and thus for design purposes in the aircraft industry, the results from the ATTAS/ VFW-614 and Fokker F100 free-flight experiments are available [49–51]. There, for Tollmien–Schlichting transition $N_{\mathrm{crit}}^{\mathrm{TS}} = N|_{x^T}^{\mathrm{TS}} \approx 12$ and for crossflow transition $N_{\mathrm{crit}}^{\mathrm{CF}} = N|_{x^T}^{\mathrm{CF}} \approx 9$ can be read, and also the shape and extent of the mixed transition region can be extracted with some accuracy.

IV. Conclusion

The Reynolds-averaged Navier–Stokes solver FLOWer coupled to a transition prediction module was applied for the first time to three-dimensional, finite wing configurations to perform RANS computations with automatic laminar–turbulent transition prediction. It could be shown that the coupled system represents a RANS-based computational fluid dynamics tool that, in principle, provides accurate values of the transition locations during the ongoing RANS computation, automatically and fast without the need for the intervention by the code user. Thus, RANS computations of three-dimensional wings with transition can be carried out without a priori knowledge of the transition characteristics of the specific flow problem.

Therefore, the characteristics of the stability boundary given by a specific correlation of the N factors for Tollmien–Schlichting transition and crossflow transition must be known with sufficient accuracy. This requirement is a shortcoming of the e^N-method when it is to be applied to configurations for which these data are not available, which is often the case for configurations tested in wind tunnels. In such a case, it is necessary to calibrate the e^N-method with respect to the critical N factor values for Tollmien–Schlichting transition and crossflow transition. This can be done by taking the N factor value corresponding to the measured transition location of one side of one wing section of one angle of attack and applying it to all other wing sections on both sides of the wing for all other angles of attack.

For one of the test cases, it was found that using laminar separation points as approximation for the real transition points due to the presence of a laminar separation bubble may lead to inaccurate transition lines. For an improvement of the results in such a case, criteria for the prediction of transition inside laminar separation bubbles will be incorporated into the transition prediction module.

Acknowledgments

This work has partly been carried out within the European High Lift Program (EUROLIFT 2 project) [52]. The EUROLIFT II project is a collaboration between DLR, German Aerospace Center, Airbus-Deutschland, Airbus-France, Airbus-United Kingdom, Alenia Aeronautica, ICAROS Computing, Dassault Aviation, Centro Italiano Ricerche Aerospaziali, European Transonic Wind Tunnel, Engineer, Büro Kretschmar, Instituto Nacional de Tecnica Aeroespacial, ONERA, National Aerospace Laboratory, and the Swedish Defense Research Agency. The project is managed by DLR and is partly funded by the European Union (Project Ref: GRD-2004-502896).

References

[1] Rudnik, R., Ronzheimer, A., and Schenk, M., "Berechnung von zwei- und dreidimensionalen Hochauftriebskonfigurationen durch Lösung der Navier–Stokes Gleichungen," *Deutschen Gesellschaft für Luft- und Raumfahrt (DGLR), JT 96-104, Deutscher Luft- und Raumfahrtkongreß, DGLR-Jahrestagung*, Deutsche Gesellschaft für

Luft- und Raumfahrt, Lilienthal-Oberth, DGLR, D-53175 Bonn, Germany, 1996, pp. 717–726.
[2] Smith, A. M. O., and Gamberoni, N., "Transition, Pressure Gradient, and Stability Theory," Douglas Aircraft Co., Rep. ES 26388, Long Beach, CA, 1956.
[3] van Ingen, J. L., "A Suggested Semi-Empirical Method for the Calculation of the Boundary Layer Transition Region," Univ. of Delft, Rep. VTH-74, Department of Aerospace Engineering, Delft, The Netherlands, 1956.
[4] Arnal, D., and Casalis, G., "Laminar-Turbulent Transition Prediction in Three-Dimensional Flows," *Progress in Aerospace Sciences*, Vol. 36, 2000, pp. 173–191.
[5] Radespiel, R., Graage, K., and Brodersen, O., "Transition Predictions Using Reynolds-Averaged Navier–Stokes and Linear Stability Analysis Methods," AIAA Paper 91-1641, 1991.
[6] Stock, H. W., and Haase, W., "A Feasibility Study of e^N Transition Prediction in Navier–Stokes Methods for Airfoils," *AIAA Journal*, Vol. 37, No. 10, 1999, pp. 1187–1196.
[7] Horton, H. P., and Stock, H. W., "Computation of Compressible, Laminar Boundary Layers on Swept, Tapered Wings," *Journal of Aircraft*, Vol. 32, No. 6, 1995, pp. 1402–1405.
[8] Stock, H. W., and Degenhardt, E., "A Simplified e^N Method for Transition Prediction in Two-Dimensional, Incompressible Boundary Layers," *Zeitung für Flugwissenschaft und Weltraumforschung*, Vol. 13, 1989, pp. 16–30.
[9] Casalis, G., and Arnal, D., "ELFIN II Subtask 2.3: Database method: Development and Validation of the Simplified Method for Pure Crossflow Instability at Low Speed," ONERA-CERT, TR-145; also DERAT No. 119/5618.16, Département d'Études et de Recherches en Aérothermodynamique (DERAT), ELFIN II: European Laminar Flow Investigation, Toulouse, France, Dec. 1996.
[10] Crouch, J. D., Crouch, I. W. M., and Ng, L. L., "Transition Prediction for Three-Dimensional Boundary Layers in Computational Fluid Dynamics Applications," *AIAA Journal*, Vol. 40, No. 8, 2002, pp. 1536–1541.
[11] Warren, E. S., and Hassan, H. A., "Transition Closure Model for Predicting Transition Onset," *Journal of Aircraft*, Vol. 35, No. 5, 1998, pp. 769–775.
[12] Czerwiec, R. M., Edwards, J. R., Rumsey, C. L., Bertelrud, A., and Hassan, H. A., "Study of High-Lift Configurations Using k–ζ Transition/Turbulence Model," *Journal of Aircraft*, Vol. 37, No. 6, 2000, pp. 1008–1016; also AIAA Paper 99-3186, 1999.
[13] Edwards, J. R., Roy, C. J., Blottner, F. G., and Hassan, H. A., "Development of a One-Equation Transition/Turbulence Model," *AIAA Journal*, Vol. 39, No. 9, 2001, pp. 1691–1698.
[14] Langtry, R. B., and Menter, F. R., "Transition Modeling for General CFD Applications in Aeronautics," AIAA Paper 2004-522, 2005.
[15] FLOWer: Installation and User Handbook, Release 116, Doc.Nr. MEGAFLOW-1001, Institut für Entwurfsaerodynamik, Deutsches Zentrum für Luft- und Raumfahrt, e. V.,, 2000.
[16] Krumbein, A., Stock, H. W., "Laminar-Turbulent Transition Modeling in Navier–Stokes Solvers Using Engineering Methods," ECCOMAS 2000, Barcelona (e), 11–14 Sept. 2000, ECCOMAS 2000: CD-ROM Proceedings, International Center for Numerical Methods in Engineering (CIMNE), 2000, ISBN: 84-89925-70-4, Depósito Legal: B-37139-2000.
[17] Krumbein, A., "Coupling of the DLR Navier–Stokes Solver FLOWer with an e^N-Database Method for Laminar-Turbulent Transition Prediction on Airfoils," *New Results in Numerical and Experimental Fluid Mechanics III*, Notes on Numerical Fluid Mechanics, Vol. 77, Springer-Verlag, Berlin, 2002, pp. 92–99.
[18] Krumbein, A., "Transitional Flow Modeling and Application to High-Lift Multi-Element Airfoil Configurations," *Journal of Aircraft*, Vol. 40, No. 4, 2003, pp. 786–794; also AIAA Paper 2003-0724, Jan. 2003.
[19] Krumbein, A., "Automatic Transition Prediction and Application to High-Lift Multi-Element Configurations," *Journal of Aircraft*, Vol. 42, No. 5, 2005, pp. 1150–1164; also AIAA Paper 2004-2543, June/July 2004.
[20] Krumbein, A., "Navier–Stokes Airfoil Computations with Automatic Transition Prediction using the DLR TAU Code: A Sensitivity Study," New Results in Numerical and Experimental Fluid Mechanics 5, *Notes on Numerical Fluid Mechanics and Multidisciplinary Design*, Springer–Verlag, Berlin, 2006, pp. 192–199.
[21] Krumbein, A., "Automatic Transition Prediction for High-Lift Systems Using a Hybrid Flow Solver," *Journal of Aircraft*, Vol. 42, No. 5, 2005, pp. 1362–1366.
[22] Nebel, C., Radespiel, R., and Wolf, T., "Transition Prediction for 3D Flows Using a Reynolds-Averaged Navier–Stokes Code and N-Factor Methods," AIAA Paper 2003-3593, 2003.
[23] Arthur, M. T., Dol, H., Krumbein, A., Houdeville, R., and Ponsin, J., "Application of Transition Criteria in Navier–Stokes Computations," ONERA, GARTEUR Transition Action Group AD (AG-35), TP137, Toulouse, France, Jan. 2003.
[24] Stock, H. W., and Krumbein, A., "2D High-Lift RANS Computations with e^N Transition Prediction: A310 Take-Off and Landing Configurations," Deutsches Zentrum für Luft- und Raumfahrt (DLR) , Rept. HiAer D1.3-2, Braunschweig, Germany, April 2003.
[25] Stock, H. W., "Navier–Stokes Computations of Laminar Airfoils Using e^N Transition Prediction," Deutsches Zentrum für Luft- und Raumfahrt (DLR), Internal Rept. IB 129-99, Braunschweig, Germany, 18 Aug. 1999.
[26] Stock, H. W., "Infinite Swept Wing RANS Computations with e^N Transition Prediction, a Validation Study," Deutsches Zentrum für Luft- und Raumfahrt (DLR), Rept. ALTTA D3.1.2-4, Braunschweig, Germany, Oct. 2002.
[27] Stock, H. W., and Haase, W., "Some Aspects of Linear Stability Calculations in Industrial Applications," *Transitional Boundary Layers in Aeronautics*, edited by Henkes, R. A. W. M., and van Ingen, J. L., North-Holland, Amsterdam, 1996, pp. 225–238.
[28] Arnal, D., "Transition Prediction in Transonic Flow," *Symposium Transsonicum III, IUTAM Symposium*, edited by Zierep, J., and Oertel, H., Springer-Verlag, Berlin, 1989, pp. 253–262.
[29] Arnal, D., "Transition de la Couche Limite," ONERA/CERT, Internal Rept. 37/5018 DY, Toulouse, France, 1987.
[30] Rozendaal, R. A., "Natural Laminar Flow Flight Experiments on a Swept Wing Business Jet-Boundary-Layer Stability Analysis," NASA CP 3975, March 1986.
[31] Rozendaal, R. A., "Variable-Sweep Transition Flight Experiment (VSTFE): Parametric Pressure Distribution Boundary-Layer Stability Study and Wing Glove Design Task," NASA CR 3992, Dec. 1986.
[32] Rozendaal, R. A., "Variable-Sweep Transition Flight Experiment (VSTFE): Stability Code Development and Clean-Up Glove Analysis," NASA CP 2847, April 1987.
[33] Stock, H. W., "Infinite Swept Wing RANS Computations with e^N Transition Prediction: Feasibility Study," Deutsches Zentrum für Luft- und Raumfahrt (DLR), Internal Rept. IB 124-2003/12, Braunschweig, Germany, Aug. 2002.
[34] Dhawan, S., and Narasimha, R., "Some Properties of Boundary Layer Flow During the Transition from Laminar to Turbulent Motion," *Journal of Fluid Mechanics*, Vol. 3, 1958, pp. 418–436.
[35] Stock, H. W., and Haase, W., "Navier–Stokes Airfoil Computations with e^N Transition Prediction Including Transitional Flow Regions," *AIAA Journal*, Vol. 38, No. 11, 2000, pp. 2059–2066.
[36] Walker, G. J., "Transitional Flow on Axial Turbomachine Blading," *AIAA Journal*, Vol. 27, No. 5, 1989, pp. 595–602.
[37] Krumbein, A., "Automatic Transition Prediction and Application to 3D Wing Configurations," AIAA Paper 2006-914, June 2006.
[38] Schmitt, V., and Charpin, F., "Pressure Distributions on the ONERA-M6-Wing at Transonic Mach Numbers," AGARD Advisory Rept. No. 138, 1979, pp. B1-1–B1-44.
[39] Baldwin, B. S., and Lomax, H., "Thin-Layer Approximation and Algebraic Model for Separated Turbulent Flows," AIAA Paper 78-257, 1978.
[40] Spalart, P. R., and Allmaras, S. R., "A One-Equation Turbulence Model for Aerodynamic Flows," *La Recherche Aérospatiale*, No. 1, 1994, pp. 5–21.
[41] Edwards, J. R., and Chandra, S., "Comparison of Eddy Viscosity: Transport Turbulence Models for Three-Dimensional, Shock-Separated Flowfields," *AIAA Journal*, Vol. 34, No. 4, 1996, pp. 756–763.
[42] Wilcox, D. C., "Reassessment of the Scale-Determining Equation for Advanced Turbulence Models," *AIAA Journal*, Vol. 26, No. 11, 1988, pp. 1299–1310.
[43] Surana, A., Grunberg, O., and Haller, G., "Exact Theory of Three-Dimensional Flow Separation. Part I: Steady Separation," *Journal of Fluid Mechanics*, article in press, 5 July 2006 (http://jfm-www.damtp.cam.ac.uk/In_Press.html).
[44] Schmitt, V., and Cousteix, J., "Étude de la couche limite tridimensionelle sur une aile en flèche," ONERA, No. TR 14/1713 AN, Châtillon, France, July 1975.
[45] Schmidt, G. S., and Mueller, Th. J., "Analysis of Low Reynolds Number Separation Bubbles Using Semi-Empirical Methods," *AIAA Journal*, Vol. 27, No. 8, 1989, pp. 993–1001.
[46] Redeker, G., and Wichmann, G., "Forward Sweep: A Favorable Concept for a Laminar Flow Wing," *Journal of Aircraft*, Vol. 28, No. 2, 1991, pp. 97–103.

[47] Stock, H. W., "Infinite Swept-Wing Navier–Stokes Computations with e^N Transition Prediction," *AIAA Journal*, Vol. 43, No. 5, June 2005, pp. 1221–1229.

[48] Sobieczky, H., "DLR F5: Test Wing for CFD and Applied Aerodynamics," Test Case B-5, *Test Cases for CFD Validation*, AGARD Advisory Rept. No. AR 303, 1994, pp. B5-1–B5-16.

[49] Schrauf, G., Perraud, J., and Lam, F., "Comparison of Boundary-Layer Transition Predictions Using Flight Test Data," *Journal of Aircraft*, Vol. 35, No. 6, 1998, pp. 891–897.

[50] Schrauf, G., and Atkin, Ch., "Progress in Linear Stability Methods for Design Applications," ECCOMAS 2000, Barcelona (e), 11–14 Sept. 2000, CD-Rom Proceedings, Editor: International Center for Numerical Methods in Engineering (CIMNE), 2000, ISBN: 84-89925-70-4, Depósito Legal: B-37139-2000.

[51] Schrauf, G., "Large-Scale Laminar-Flow Tests Evaluated with Linear Stability Theory," *Journal of Aircraft*, Vol. 41, No. 2, 2004, pp. 224–230.

[52] EUROLIFT 2-European High-Lift Program 2, Annex B: Description of Work, Specific Targeted Research Project of the 6th European Framework Program, GRD-2004-502896, 2004.